A Novel PCB-Embedded Coupled Inductor Structure for Integrated Voltage Regulator

Feiyang Zhu, Qiang Li and Fred C. Lee

The Bradley Department of Electrical and Computer Engineering Virginia Polytechnic Institute and State University, Blacksburg, VA, USA feiyz94@vt.edu

Abstract—As portable devices become smaller and thinner, an integrated voltage regulator (IVR) can save space and improve the efficiency of the whole system dramatically, thereby becoming a promising solution to power microprocessors. However, its highfrequency magnetic design is quite challenging and usually becomes the bottleneck. In previous work, a novel, two-phase coupled inductor structure with unsymmetrical through-core conductor distribution was demonstrated as a good candidate due to its small loss, footprint, and low profile. In this paper, the unique coupling mechanism of this specific structure is revealed, based on an equivalent circuit model to fully explore its benefits. Then, a four-phase integrated inductor is proposed to further improve inductor performance by utilizing flux cancellation. To realize a fully integrated three-dimensional IVR, PCB-embedded inductor samples are fabricated and tested experimentally. Compared with other state-of-art solutions, the proposed inductor structure integrates four inductors into one magnetic core with much smaller dc resistance and large inductance density.

Keywords— integrated voltage regulator, coupled inductor, integrated magnetics, PCB integration

I. INTRODUCTION

As power demands of microprocessors in portable devices (e.g., smartphones) continuously grow, high power density voltage regulator design becomes more and more important to address space constraints. In today's products, substantial space on the motherboard is occupied by passive components of multiphase voltage regulators with relatively low-frequency operation. By pushing switching frequency to tens of Megahertz, an integrated voltage regulator (IVR) [1]-[5] is a promising solution to save space and increase power density dramatically. Due to its smaller size, the integrated voltage regulator can be placed very close to the microprocessor, thus providing faster transient speed and improving the efficiency of the whole system.

High-frequency inductor design and integration are the main challenges to realize the IVR. Different high-frequency magnetic structures are proposed in [5]-[23]; most of them are single-phase, non-coupled inductor structures. Compared with non-coupled inductors, a negative coupled inductor can realize small steady-state current ripple and fast transient speed at the same time [24]. A two-phase negative coupled inductor with a stripline core shape was proposed in [7]. Due to negative coupling, dc flux in the core is reduced and higher saturation

current level is achieved; however, the leakage flux flowing in the air may cause a noise issue. Also, it is difficult to achieve large inductance with a small inductor size due to its single-turn structure. A multi-turn two-phase coupled inductor structure with a lateral flux pattern was proposed in [20]. High inductance density can be achieved regardless of magnetic core thickness, and almost all of the flux are well confined in the core in this structure. However, additional low-permeability magnetic material needs to be added into the air slots to maintain large steady-state inductance and small transient inductance under different load currents. [6] and [12] proposed a three or fourphase coupled inductor structure. Each phase is coupled with another two phases to achieve better circuit performance compared with the two-phase coupled inductor; however, the winding length of each inductor is long and results in large dc resistance (DCR). Each phase inductor requires a separate magnetic piece which increases fabrication cost. In [10], a fourphase integrated coupled inductor with a ladder core shape was proposed, but the inherent unsymmetrical coupling property of this structure results in a phase current ripple difference and larger output voltage ripple. Therefore, a multi-phase coupled inductor structure with symmetrical coupling, short winding length, low profile and integrated magnetics is required for IVR design.

In [21], a novel, two-phase, negative coupled inductor structure for a three-dimensional integrated voltage regulator was proposed and is shown in Fig. 1. Each inductor winding is composed by using three through-core conductors together with two surface windings. The inductor is directly beneath the microprocessor to provide a very short vertical power delivery path and small parasitic impedance. Negative coupling reduces the dc flux in the core and boosts inductance. It has been demonstrated that this structure can achieve very small DCR, inductor loss, and footprint, with low profile and large current handling ability; however, the coupling mechanism of this structure has not yet been analyzed. A multi-phase integrated magnetic structure, as well as the inductor integration method, need to be further explored.

This paper is organized as follows. The coupling mechanism of this inductor structure is analyzed in detail in Section II. Then, a four-phase integrated inductor structure is proposed in Section III to further improve the inductor performance by flux cancellation. In Section IV, a PCB-embedded inductor is

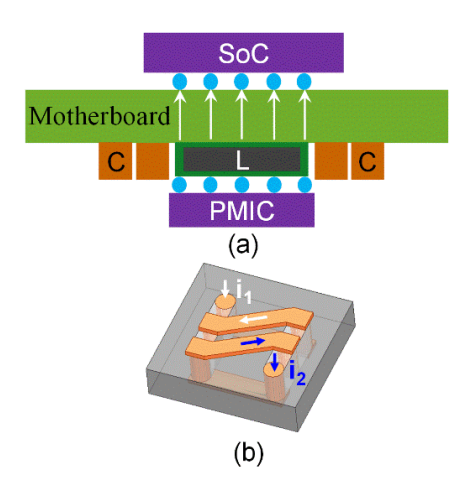


Fig. 1. (a) Three-dimensional integrated voltage regulator. (b) Two-phase coupled inductor structure with unsymmetrical through-core conductor distribution.

designed based on the proposed inductor structure. Finally, inductor performances are tested experimentally in Section V.

II. COUPLING ANALYSIS OF COUPLED INDUCTOR WITH UNSYMMETRICAL THROUGH-CORE CONDUCTOR DISTRIBUTION

A. Flux Distribution

Fig. 2(a) shows the two-phase coupled inductor structure with unsymmetrical through-core conductor distribution. The upper three through-core conductors belong to one inductor, L_{I} , and the lower three conductors make up another inductor, L_2 . For each inductor, since the number of conductors in each slot is different, the through-core conductor distribution is unsymmetrical. The cross on the conductor represents current flowing into the paper, and the dot indicates the current flowing out of the paper. The flux path of L_1 and L_2 are represented by green and blues lines, respectively. In each half of the magnetic core, the flux directions of the two inductors are opposite which forms negative coupling; therefore, dc flux in the core is reduced due to cancellation. Furthermore, the flux interaction between the two halves of the core results in an even weaker dc flux in the middle area of the core, as shown in Fig. 2(b). Since there is no air gap on the flux path in this structure, the dc flux level impacts the permeability of the magnetic material and inductance. Negative coupling results in smaller dc flux and helps boost the inductance density for this structure. Due to an interleaving effect, the ac flux in the middle area of the core also becomes weaker, as shown in Fig. 2(b). Therefore, the middle area of the core can be further optimized to achieve better core utilization.

B. Coupling Analysis

Due to unsymmetrical through-core conductor distribution, the coupling mechanism of this structure is quite unique and needs further analysis. Fig. 3 shows the equivalent circuit model of the coupled inductor structure. According to the flux pattern, each inductor is seen as two small inductors in series:

$$L_{1} = L_{1a} + L_{1b} \tag{1a}$$

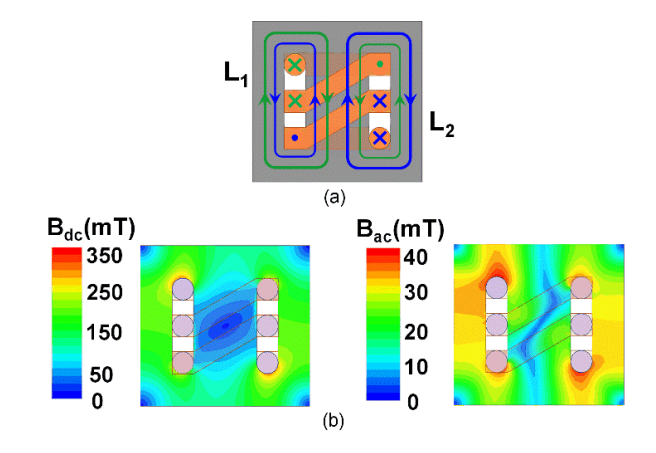


Fig. 2. (a) Two-phase coupled inductor structure (green: flux path of L₁; blue: flux path of L₂). (b) DC and AC flux distribution in the core.

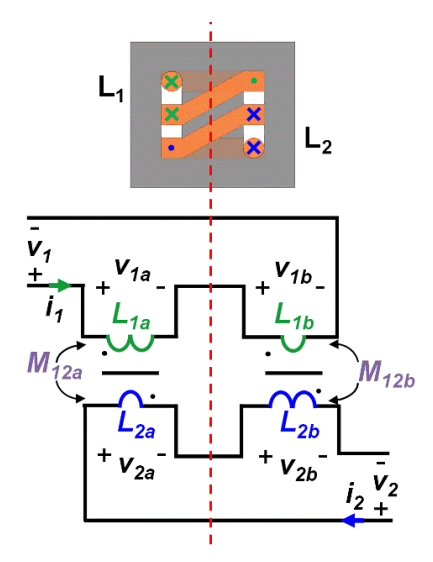


Fig. 3. Equivalent circuit model of coupled inductor with unsymmetrical through-core conductor distribution.

$$L_2 = L_{2a} + L_{2b} (1b)$$

where L_{Ia} is the inductance of two conductors in L_I in the left part of the core, L_{lb} is the inductance of the conductor in L_l in the right part of the core, L_{2a} is the inductance of the conductor in L_2 in the left part of the core, and L_{2b} is the inductance of two conductors in L_2 in the right part of the core. In each half of the core, there is

$$\begin{bmatrix} v_{1a} \\ v_{2a} \end{bmatrix} = \begin{bmatrix} L_{1a} & M_{12a} \\ M_{12a} & L_{2a} \end{bmatrix} \begin{bmatrix} \frac{di_1}{dt} \\ \frac{di_2}{dt} \end{bmatrix}$$

$$\begin{bmatrix} v_{1b} \\ v_{2b} \end{bmatrix} = \begin{bmatrix} L_{1b} & M_{12b} \\ M_{12b} & L_{2b} \end{bmatrix} \begin{bmatrix} \frac{di_1}{dt} \\ \frac{di_2}{dt} \end{bmatrix}$$
(2a)

$$\begin{bmatrix} v_{1b} \\ v_{2b} \end{bmatrix} = \begin{bmatrix} L_{1b} & M_{12b} \\ M_{12b} & L_{2b} \end{bmatrix} \begin{bmatrix} \frac{di_1}{dt} \\ \frac{di_2}{dt} \end{bmatrix}$$
 (2b)

where v_{1a} , v_{1b} , v_{2a} and v_{2b} are voltages across L_{1a} , L_{1b} , L_{2a} and L_{2b} , i_1 , and i_2 are inductor currents of L_1 and L_2 . We also have the following:

$$v_1 = v_{1a} + v_{1b} (3a)$$

$$v_2 = v_{2a} + v_{2b} \tag{3b}$$

In each half of the core, we assume two inductors from L_1 and L_2 are tightly coupled with each other, and the flux flowing through the air slots can be neglected. Then,

$$L_{1a} = L_{2b} = \frac{4}{R_{core}} \tag{4a}$$

$$L_{1b} = L_{2a} = \frac{1}{R_{core}}$$
 (4b)

$$M_{12a} = M_{12b} = -\frac{2}{R_{core}}$$
 (4c)

where R_{core} is the equivalent reluctance in each half of the core. Substituting (2) and (4) into (3) yields an inductance matrix:

$$\begin{bmatrix} v_1 \\ v_2 \end{bmatrix} = \begin{bmatrix} \frac{5}{R_{core}} & -\frac{4}{R_{core}} \\ -\frac{4}{R_{core}} & \frac{5}{R_{core}} \end{bmatrix} \begin{bmatrix} \frac{di_1}{dt} \\ \frac{di_2}{dt} \end{bmatrix}$$
 (5)

Therefore,

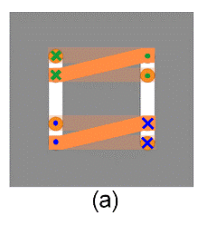
$$L_{self} = \frac{5}{R_{core}} \tag{6a}$$

$$M = -\frac{4}{R_{\text{core}}} \tag{6b}$$

$$\alpha = \frac{M}{L_{self}} = -0.8 \tag{6c}$$

where L_{self} , M and α are the self inductance, mutual inductance and coupling coefficient of this coupled inductor. It is seen that the maximum coupling coefficient of this structure is always less than one. Therefore, the distance between L_1 and L_2 can be reduced to achieve a small inductor size without changing this coupled inductor into a transformer.

As shown in Fig. 4, [19] and [20] proposed other coupled inductor structures with symmetrical conductor distribution. The number of conductors in each slot for each inductor are the same. According to previous analysis, the coupling coefficient of the inductor structure in Fig. 4(a) is very close to one due to symmetrical conductor distribution. This results in small steady-state inductance and large current ripple. The distance between the two inductors needs to be increased to reduce coupling but has the tradeoff of a larger inductor footprint. To solve this issue, [20] proposed adding low permeability magnetic material into the air slots as shown in Fig. 4(b). More flux flows through the core area between the two inductors. This is created by low permeability magnetic material, which keeps the coupling coefficient in a reasonable range. However, adding low permeability material into slots increases fabrication cost and



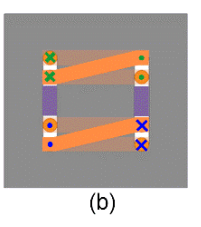


Fig. 4. Coupled inductor structure with symmetrical conductor distribution:

(a) inductor with air slots and (b) inductor with slots filled by low permeability magnetic material.

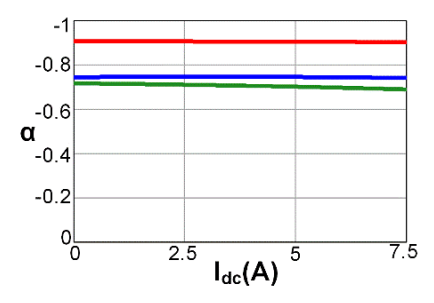


Fig. 5. Coupling coefficient comparison of different coupled inductor structures (red:inductor structure in Fig.4(a)); green: inductor structure in Fig.4(b); blue: inductor with unsymmetrical conductor distribution).

may not be practical if the slots are too short or narrow. Fig. 5 shows the coupling coefficient comparison between different inductor structures based on Maxwell simulation results. It shows that by changing conductor distribution, the inductor structure with unsymmetrical conductor distribution achieves a similar coupling coefficient in a simpler structure compared with the structure in Fig. 4(b).

III. PROPOSED FOUR-PHASE INTEGRATED INDUCTOR STRUCTURE

As power demand of microprocessors continuously grows, multi-phase buck converters with multi-phase inductors, are required to deliver the power. Compared with discrete inductors, the multi-phase integrated inductor has the opportunity to improve inductor performance and reduce fabrication cost. The most straightforward way to build a four-phase integrated inductor based on the basic inductor unit in Fig. 2(a) is by merging two of these units into one magnetic piece, as shown in Fig. 6(a). The benefit of integration is that both dc and ac flux density in the core area between the two units becomes weaker due to flux cancellation, compared with that of the single unit case. Therefore, the parameter d, which controls the distance between the two units, can be further reduced to shrink the unutilized core area. The inductor loss and footprint are evaluated by sweeping d with g=0.44 mm, as shown in Fig. 7. The circuit parameters are as follows: input voltage V_{in} =3.8 V, output voltage $V_o=1$ V, and switching frequency $f_s=20$ MHz. The property of magnetic material from TOKIN is characterized by a high-frequency core loss method [18], [25] and imported into Maxwell software to simulate inductor loss. From Fig. 7, it is seen that a smaller d value reduces the unutilized core area and inductor footprint with very little increased core loss. However,

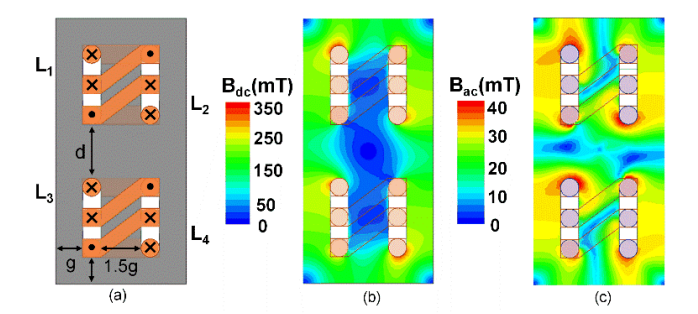


Fig. 6. (a) Proposed four-phase integrated inductor structure. (b) DC flux density distribution in the core. (c) AC flux density distribution in the

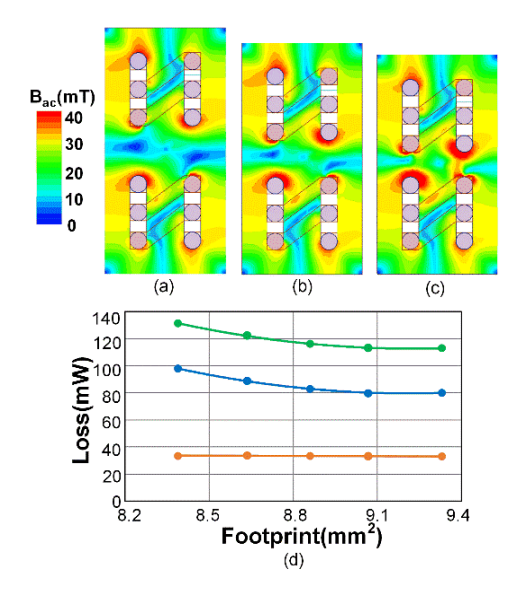


Fig. 7. AC flux distribution with (a) d=2g (b) d=1.5g (c) d=g (d) Inductor loss(per phase) and footprint under different d values.

ac flux starts crowding in the middle of the core area and results in larger ac flux density and noticeable increased core loss if d is too small. Therefore, the inductor structure in Fig. 7(b) can be chosen as an optimal point where a smaller inductor footprint is achieved with a negligible core loss increase.

IV. DESIGN OF PCB-EMBEDDED INTEGRATED COUPLED INDUCTOR

To realize a fully integrated voltage regulator, the inductor is either embedded into a silicon wafer or an organic interposer, such as a printed circuit board (PCB). Today's microprocessors in smartphones require more than ten amperes current and will require even more in the future. Therefore, PCB embedding technology is applied for the proposed inductor structure to handle such large load current. According to the specifications in smartphones, the nominal operating voltage of V_{in} =3.8 V and V_o =1 V in buck converters is used for inductor design. The switching frequency is designed at 20 MHz. The four-phase inductor is designed to support maximum 15 A load current. Magnetic material from TOKIN is used due to its high permeability, low loss, and compatibility with the PCB

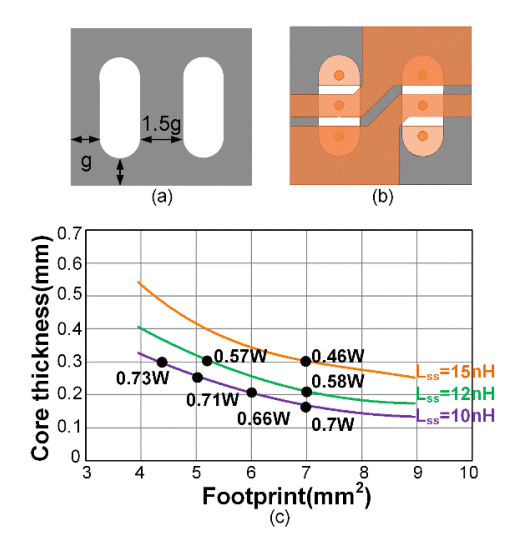


Fig. 8. (a) Dimension of magnetic core in two-phase coupled inductor. (b) Two-phase coupled inductor with windings. (c) Inductor size and total loss evaluation of two-phase coupled inductor with different steady-state inductances at 7.5A load current.

TABLE I. DESIGN RESULTS OF FOUR-PHASE INTEGRATED INDUCTOR

Design results	Value		
Steady-state indcutance(L_{ss})	15nH		
Transient indcutance(L_{tr})	7nH		
DC resistance(DCR)	2.8mΩ		
Core loss	0.68W		
Winding loss	0.21W		
Inductor total loss	0.89W		
Core thickness	0.3mm		
Core length	4.71mm		
Core width	2.86mm		

manufacturing process [17]. The material property is characterized by a high-frequency core loss measurement method [18], [25] and built into Maxwell software to simulate inductor loss.

First, the performance of the two-phase coupled inductor is evaluated. Fig. 8(a) and Fig. 8(b) show the core dimension and the whole structure with windings. PCB copper-filled vias are used as through-core conductors, and their diameters are 0.15 mm. The copper thickness of the surface windings is 0.05 mm. The width of air slots in the core is 0.65 mm. By sweeping parameter g in Fig. 8(a), the cross-section area of the core and inductor footprint are changed as well as inductor loss. The simulated core thickness, footprint, and inductor loss with different inductances are shown in Fig. 8(c). Each curve corresponds to a steady-state inductance value that varies from 10 nH to 15 nH. With a given inductance, the inductor footprint decreases with larger core thickness, and the inductor loss varies little. For a given footprint, inductor loss is reduced with larger core thickness due to smaller core loss.

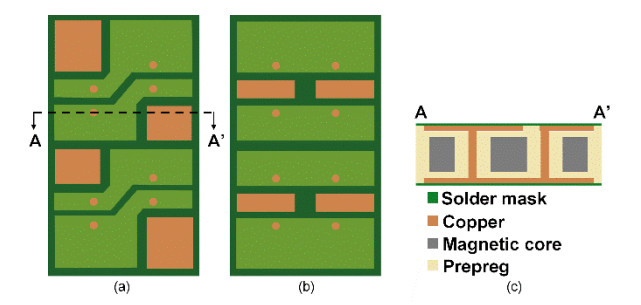


Fig. 9. PCB-embedded four-phase integrated inductor structure: (a) top view (b) bottom view (c) cross-section view.



Fig. 10. Fabricated PCB-embedded inductor sample.

A design example with a 7 mm² footprint and 0.3 mm core thickness for this two-phase coupled inductor is chosen to meet the stringent space requirement in smartphones. Following the same optimization process in Section III, the design results of the four-phase integrated inductors at 15A load current are listed in TABLE I. Due to negative coupling, large steady-state inductance and small transient inductance are achieved to realize small steady-state current ripple and fast transient speed. The footprint of this four-phase inductor is only 13.5 mm² with 0.3 mm core thickness. Then, this inductor is sandwiched into a two-layer PCB using a conventional PCB laminating process. The layer stack-up of the PCB-embedded inductor is shown in Fig. 9. The inductor samples are fabricated for hardware tests as shown in Fig. 10. The dimension of this PCB-embedded inductor is 5.21x3.36x0.54mm. The experimental results are presented in Section V.

V. EXPERIMENTAL RESULTS

A. Inductance Measurement

First, the inductance of the PCB-embedded inductor samples is measured to verify the design. Since there is no air gap in the flux path, the permeability of magnetic material changes with load current, which results in inductance change. Therefore, the inductance under different dc current levels needs to be characterized. According to the previous analysis, the coupling between two inductor cells in the four-phase inductor structure is very weak and can be neglected. Fig. 11 shows the dc magnetic field intensity distribution under two different excitation conditions. It indicates that the dc magnetic field intensity in the top inductor cell is not impacted by the dc current excitations in the other inductor cell. Therefore, this four-phase inductor can be treated as a two-phase coupled inductor from an inductance point of view to simplify the measurement setup. Fig. 12 shows the principle of the inductance measurement method. Each dc current source is connected to one inductor to provide de currents. An AC excitation source (e.g., function generator with power amplifier) is only applied to one inductor,

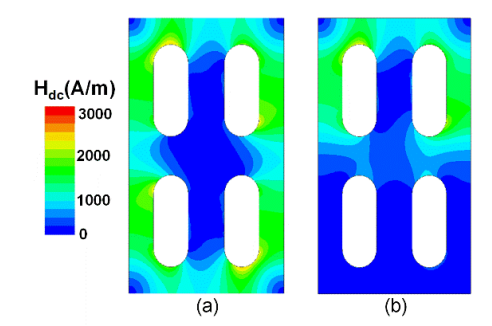


Fig. 11. Simulated DC magnetic field intensity in the core. (a) Each inductor is applied with 3.75A dc current. (b) Only top two inductors are applied with 3.75A dc current.

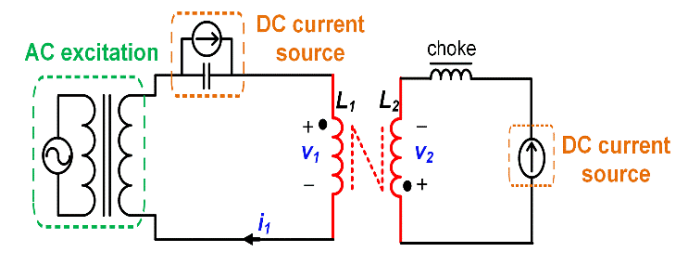


Fig. 12. Inductance measurement method of two-phase coupled inductor.

and the other inductor is open from an ac signal point of view. Then, the inductances of each inductor can be calculated based on measured voltages and currents:

$$L_{self} = \frac{1}{2\pi f} \frac{V_1}{I_1}$$
 (7a)

$$\left| M \right| = \frac{1}{2\pi f} \frac{V_2}{I_1} \tag{7b}$$

where V_1 and V_2 are the voltage amplitudes on L_1 and L_2 respectively, I_1 is the amplitude of ac current flowing through L_1 , and f is the frequency of ac excitation source.

Fig. 13 shows the measured inductances of three different inductor samples under 20MHz excitation frequency and different dc currents. The measurement results match very well with the simulation results from Maxwell, which verifies the design and proves that the PCB integration has no impact on inductor performance. Based on the self inductance and mutual inductance, the steady-state inductance and transient inductance are calculated as follows:

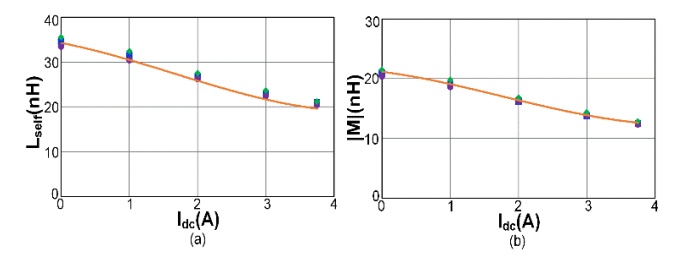


Fig. 13. (a) Measured self inductance. (b) Measured mutual inductance (points: measurement results of three different inductor samples; solid lines: simulation results).

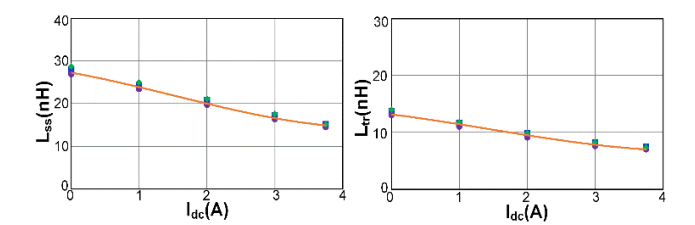


Fig. 14. Lss and Ltr under different dc currents(points: calculated Lss and Ltr based on measured L_{self} and M; lines: simulated L_{ss} and L_{tr}).

$$L_{ss} = \frac{L_{self}^2 - M^2}{L_{self} + M \frac{D}{1 - D}}$$

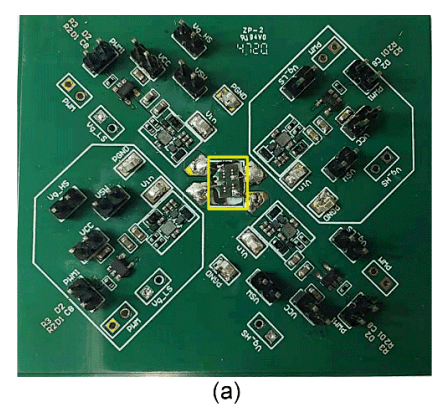
$$L_{tr} = L_{self} + M$$
(8b)

$$L_{tr} = L_{self} + M \tag{8b}$$

Fig. 14 shows calculated L_{ss} and L_{tr} based on measurement results under different dc currents. The steady-state inductance increases from heavy load to light load, which helps improve the light load efficiency.

B. Thermal Test

The thermal performance of the PCB-embedded inductor is evaluated on a four-phase buck board, as shown in Fig. 15. The low-voltage GaN switching device, EPC2040, and the gate driver PE29102 from pSemi, are soldered on the top surface of the motherboard. Output capacitors are placed on the bottom of



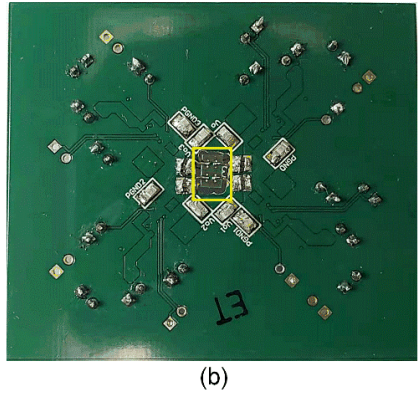


Fig. 15. Four-phase buck board with a PCB-embedded inductor in the middle of the board. (a) Top view. (b) Bottom view.

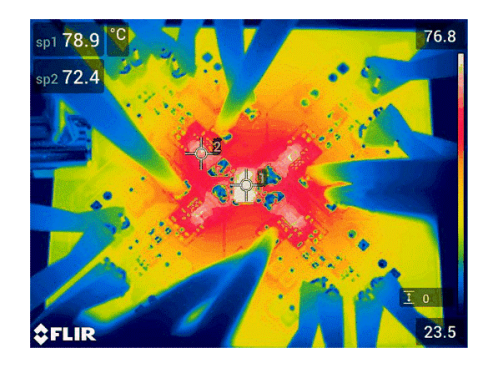


Fig. 16. Thermal test of PCB-embedded inductor at natural convection with 12 A load current(spot 1: inductor; spot 2: device).

TABLE II. INDUCTOR PERFORMANCE COMPARISON

	[13]	[14]	[15]	[16]	[22]	[23]	This work
Substrate	PCB	PCB	PCB	PCB	PCB	PCB	PCB
# of phases	1	1	1	1	1	1	4, negative coupled
F _s (MHz)	>10	20	100	10	2	>10	20
Footprint /phase(mm²)	7.25	10.2	13.2	2.5	87	25	4.4
Height(mm)	1.46	2.3	0.5	>1.8	>0.4	0.35	0.54
Inductance density (nH/mm³)	4.91	6.39	4.24	<7.33	<22.4	0.57	14.30
$R_{\text{dc}}(m\Omega)$	102	/	19	30	66	3.3	2.8

a. The self inductance at 0A is used to calculate inductance density for this work

the motherboard. A rectangular slot is drilled in the middle of the motherboard for placement of the PCB-embedded inductor. Finally, the inductor is connected to the switching nodes and output capacitors by very short external wires. Fig. 16 shows the thermal test result with V_{in} =3.8 V, V_o =1 V, f_s =20 MHz, 12A load current and natural convection condition. The black tape is attached on the surface of the inductor sample to increase the measurement accuracy of the thermal camera [26]. The inductor temperature rise is 55.4 °C. Therefore, the proposed inductor structure is thermally manageable to handle large power with the small inductor size.

TABLE II shows this inductor performance comparison with other works. Compared with single-phase inductor solutions, this work integrates four inductors into one magnetic core with negative coupling. Meanwhile, the proposed inductor structure has either larger inductance density or much smaller DCR compared with other works, demonstrating that the proposed inductor structure is a promising solution for IVR.

VI. CONCLUSION

In this paper, the coupling mechanism of a novel, two-phase coupled inductor structure is revealed, based on an equivalent circuit model to fully explore its benefits. Then, a four-phase integrated inductor is proposed to further improve inductor performance by utilizing flux cancellation. To realize a fully integrated three-dimensional IVR, a PCB-embedded inductor is designed and analyzed. Finally, the inductor samples are fabricated and tested. The measurement results match well with the design values, and the thermal test proves that the proposed inductor structure is thermally manageable to handle large power in a small inductor size. Compared with other state-of-art solutions, the proposed inductor structure has either larger inductance density or much smaller DCR, thus making it a promising solution for IVR.

ACKNOWLEDGMENT

This material is based upon work supported by the National Science Foundation under Award No. 1653156. The authors would like to thank TOKIN for providing magnetic core samples and AT&S for embedding magnetic cores into the PCB.

DISCLAIMER

Any opinions, findings, and conclusions or recommendations expressed in this material are those of the author(s) and do not necessarily reflect the views of the National Science Foundation.

REFERENCES

- F. C. Lee and Q. Li, "High-Frequency Integrated Point-of-Load Converters: Overview," *IEEE Trans. Power Electron.*, vol. 28, no. 9, pp. 4127–4136, Sep. 2013, doi: 10.1109/TPEL.2013.2238954.
- [2] C. Ó. Mathúna, N. Wang, S. Kulkarni, and S. Roy, "Review of Integrated Magnetics for Power Supply on Chip (PwrSoC)," *IEEE Trans. Power Electron.*, vol. 27, no. 11, pp. 4799–4816, Nov. 2012, doi: 10.1109/TPEL.2012.2198891.
- [3] E. A. Burton et al., "FIVR Fully integrated voltage regulators on 4th generation Intel® CoreTM SoCs," in 2014 IEEE Applied Power Electronics Conference and Exposition APEC 2014, Mar. 2014, pp. 432–439. doi: 10.1109/APEC.2014.6803344.
- [4] W. Kim, M. S. Gupta, G.-Y. Wei, and D. Brooks, "System level analysis of fast, per-core DVFS using on-chip switching regulators," in 2008 IEEE 14th International Symposium on High Performance Computer Architecture, Feb. 2008, pp. 123–134. doi: 10.1109/HPCA.2008.4658633.
- [5] W. J. Lambert, M. J. Hill, K. Radhakrishnan, L. Wojewoda, and A. E. Augustine, "Package Inductors for Intel Fully Integrated Voltage Regulators," *IEEE Trans. Compon. Packag. Manuf. Technol.*, vol. 6, no. 1, pp. 3–11, Jan. 2016, doi: 10.1109/TCPMT.2015.2505665.
- [6] N. Sturcken et al., "A 2.5D Integrated Voltage Regulator Using Coupled-Magnetic-Core Inductors on Silicon Interposer," IEEE J. Solid-State Circuits, vol. 48, no. 1, pp. 244–254, Jan. 2013, doi: 10.1109/JSSC.2012.2221237.
- [7] W. J. Lambert, M. J. Hill, K. P. O'Brien, K. Radhakrishnan, and P. Fischer, "Study of Thin-Film Magnetic Inductors Applied to Integrated Voltage Regulators," *IEEE Trans. Power Electron.*, vol. 35, no. 6, pp. 6208–6220, Jun. 2020, doi: 10.1109/TPEL.2019.2948825.
- [8] H. T. Le et al., "High-Q Three-Dimensional Microfabricated Magnetic-Core Toroidal Inductors for Power Supplies in Package," IEEE Trans. Power Electron., vol. 34, no. 1, pp. 74–85, Jan. 2019, doi: 10.1109/TPEL.2018.2847439.
- [9] D. Dinulovic, M. Shousha, M. Haug, A. Gerfer, M. Wens, and J. Thone, "On-chip high performance magnetics for point-of-load high-frequency DC-DC converters," in 2016 IEEE Applied Power Electronics Conference and Exposition (APEC), Mar. 2016, pp. 3097–3100. doi: 10.1109/APEC.2016.7468306.
- [10] N. Sturcken, R. Davies, C. Cheng, W. E. Bailey, and K. L. Shepard, "Design of coupled power inductors with crossed anisotropy magnetic core for integrated power conversion," in 2012 Twenty-Seventh Annual IEEE Applied Power Electronics Conference and Exposition (APEC), Feb. 2012, pp. 417–423. doi: 10.1109/APEC.2012.6165853.
- [11] T. O'Donnell et al., "Microfabricated inductors for 20 MHz Dc-Dc converters," in 2008 Twenty-Third Annual IEEE Applied Power Electronics Conference and Exposition, Feb. 2008, pp. 689–693. doi: 10.1109/APEC.2008.4522796.

- [12] C. Feeney, N. Wang, S. Kulkarni, Z. Pavlović, C. Ó Mathúna, and M. Duffy, "Optimization of Coupled Stripline Microinductors in Power Supply on Chip Applications," *IEEE Trans. Power Electron.*, vol. 31, no. 8, pp. 5805–5813, Aug. 2016, doi: 10.1109/TPEL.2015.2497968.
- [13] D. Jordan et al., "High Q-Factor PCB Embedded Flip-Chip Inductors with Multi-Layer CZTB Magnetic Sheet for Power Supply in Package (PwrSiP)," IEEE J. Emerg. Sel. Top. Power Electron., pp. 1–1, 2020, doi: 10.1109/JESTPE.2020.2983125.
- [14] T. Fukuoka et al., "An 86% Efficiency, 20MHz, 3D-Integrated Buck Converter with Magnetic Core Inductor Embedded in Interposer Fabricated by Epoxy/Magnetic-Filler Composite Build-Up Sheet," in 2019 IEEE Applied Power Electronics Conference and Exposition (APEC), Mar. 2019, pp. 1561–1566. doi: 10.1109/APEC.2019.8722209.
- [15] M. L. F. Bellaredj, A. K. Davis, P. Kohl, and M. Swaminathan, "Magnetic Core Solenoid Power Inductors on Organic Substrate for System-in-Package Integrated High-Frequency Voltage Regulators," *IEEE J. Emerg. Sel. Top. Power Electron.*, vol. 8, no. 3, pp. 2682–2695, Sep. 2020, doi: 10.1109/JESTPE.2019.2914215.
- [16] S. Kulkarni, D. Li, D. Jordan, N. Wang, and C. Ó Mathúna, "PCB Embedded Bondwire Inductors With Discrete Thin-Film Magnetic Core for Power Supply in Package," *IEEE J. Emerg. Sel. Top. Power Electron.*, vol. 6, no. 2, pp. 614–620, Jun. 2018, doi: 10.1109/JESTPE.2018.2799238.
- [17] W. Zhang, Y. Su, M. Mu, D. J. Gilham, Q. Li, and F. C. Lee, "High-Density Integration of High-Frequency High-Current Point-of-Load (POL) Modules With Planar Inductors," *IEEE Trans. Power Electron.*, vol. 30, no. 3, pp. 1421–1431, Mar. 2015, doi: 10.1109/TPEL.2014.2320857.
- [18] D. Hou, F. C. Lee, and Q. Li, "Very High Frequency IVR for Small Portable Electronics With High-Current Multiphase 3-D Integrated Magnetics," *IEEE Trans. Power Electron.*, vol. 32, no. 11, pp. 8705– 8717, Nov. 2017, doi: 10.1109/TPEL.2016.2646702.
- [19] Yipeng Su, Dongbin Hou, F. C. Lee, and Qiang Li, "Low profile coupled inductor substrate with fast transient response," in 2015 IEEE Applied Power Electronics Conference and Exposition (APEC), Mar. 2015, pp. 1161–1168. doi: 10.1109/APEC.2015.7104494.
- [20] D. Hou, Y. Su, Q. Li, and F. C. Lee, "Improving the efficiency and dynamics of 3D integrated POL," in 2015 IEEE Applied Power Electronics Conference and Exposition (APEC), Mar. 2015, pp. 140–145. doi: 10.1109/APEC.2015.7104344.
- [21] F. Zhu, Q. Li, and F. C. Lee, "20MHz, Two Phase Negative Coupled Inductor Design for Integrated Voltage Regulator in Smartphone Applications," in 2020 IEEE Applied Power Electronics Conference and Exposition (APEC), Mar. 2020, pp. 181–187. doi: 10.1109/APEC39645.2020.9124371.
- [22] R. Murphy, Z. Pavlovic, P. McCloskey, C. O Mathuna, S. O'Driscoll, and G. Weidinger, "PCB Embedded Toroidal Inductor for 2MHz Point-of-Load Converter," in CIPS 2020; 11th International Conference on Integrated Power Electronics Systems, Mar. 2020, pp. 1–5.
- [23] J. Qiu, D. V. Harburg, and C. R. Sullivan, "A toroidal power inductor using radial-anisotropy thin-film magnetic material based on a hybrid fabrication process," in 2013 Twenty-Eighth Annual IEEE Applied Power Electronics Conference and Exposition (APEC), Mar. 2013, pp. 1660– 1667. doi: 10.1109/APEC.2013.6520520.
- [24] Pit-Leong Wong, Peng Xu, P. Yang, and F. C. Lee, "Performance improvements of interleaving VRMs with coupling inductors," *IEEE Trans. Power Electron.*, vol. 16, no. 4, pp. 499–507, Jul. 2001, doi: 10.1109/63.931059.
- [25] F. Zhu, Q. Li, and F. C. Lee, "Improved Partial Cancellation Method for High Frequency Core Loss Measurement," in 2019 IEEE Applied Power Electronics Conference and Exposition (APEC), Mar. 2019, pp. 1430– 1435. doi: 10.1109/APEC.2019.8722221.
- [26] https://www.flir.com/discover/rd-science/use-low-cost-materials-toincrease-target-emissivity/.